Open Ceramics 18 (2024) 100609

Contents lists available at ScienceDirect

Open Ceramics

journal homepage: www.sciencedirect.com/journal/open-ceramics

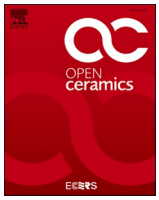

Powder-bed 3D printing by selective activation of magnesium phosphate cement: Determining significant processing parameters and their effect on mechanical strength

Farid Salari [a,*], Andrea Zocca [b], Paolo Bosetti [a], Petr Hlaváček [c], Antonino Italiano [d], Filippo Gobbin [e], Paolo Colombo [e], Hans-Carsten Kühne [c], Vincenzo M. Sglavo [a,f]

[a] Department of Industrial Engineering, University of Trento, via Sommarive 9, 38123, Trento, Italy
[b] Division Advanced Multi-Material Processing, Bundesanstalt für Materialforschung und -prüfung (BAM), Unter den Eichen 44-46, 12203, Berlin, Germany
[c] Division Technology of Construction Materials, Bundesanstalt für Materialforschung und -prüfung (BAM), Unter den Eichen 87, 12205, Berlin, Germany
[d] Desamanera Srl, Rovigo, Italy
[e] Department of Industrial Engineering, Università degli Studi di Padova, Padova, Italy
[f] INSTM, Trento Research Unit, via G. Giusti 9, 50121, Firenze, Italy

ARTICLE INFO

Handling Editor: Jens Guenster

Keywords:
Binder jetting
Concrete 3D-printing
Particle-bed binder jetting
Design of experiment
Process parameters

ABSTRACT

The present work addresses powder bed binder jetting additive manufacturing by selective magnesium phosphate cement activation. Despite the potential of this technology to aid the digitalization of the construction industry, the effect of processing parameters on the mechanical performance of printed materials has not yet been studied to generate a guideline for the further development of the technology. Statistical methodologies were used to screen the effect of four printing process parameters (printing speed, layer thickness, raster angle, and build direction on flexural and compressive strength). As the exploited technology works with constant fluid pressure, the physical interpretation of the effect of each factor can be considered taking into account the interactions between the binder materials in the powder bed. Analysis of variance (ANOVA) indicated that printing speed and layer thickness significantly affect mechanical performances. Furthermore, the layout of samples for the printing process is preferable to be parallel the printhead movement. An anisotropic behavior was observed, and the samples subjected to compressive forces parallel to the layer plane possessed lower strength values. This effect can be interpreted as a result of a weak area of low density in between layers, leading to a pronounced delamination under compression.

Even though the strength of the printed material is not suitable for a structural concrete, it can be marginally improved by design of experiment and optimized for non-structural applications, such as for porous artificial stone. Design of experiment coupled with ANOVA methods can be used in the future to support the development of novel material mixtures, thus expanding the fields of application of this novel additive manufacturing technology.

1. Introduction

The construction industry is one of the most relevant engineering fields that has been trying to adopt the industry 4.0 approach in recent years [1,2]. A promising way of supporting digital fabrication in this field is by additive manufacturing (AM) technologies. Out of the seven AM classes defined by ISO 17296-2 [3], material extrusion and binder jetting techniques are the most promising ones for on-site and large-scale projects [1,2,4]. Precast elements with high geometrical accuracy can be fabricated through powder bed solutions [2,5]. These additive manufacturing techniques may reduce production costs, increase workforce safety, enable rapid construction with local raw materials during emergencies and allow for a much wider range of shapes to be manufactured at a competitive cost [6].

Binder jetting is a powder bed bonding technique that creates objects from a CAD file, layer by layer [7]. A 3D model is required to be sliced into thin layers in a readable file format by the printer machine [8,9]. For a complete cycle, a layer of powder feedstock is deposited on the

* Corresponding author.
E-mail address: farid@concr3de.com (F. Salari).

https://doi.org/10.1016/j.oceram.2024.100609
Received 12 December 2023; Received in revised form 10 May 2024; Accepted 14 May 2024
Available online 15 May 2024

platform; then, the liquid bonding agent is sprayed on the surface of the powder bed in selected areas, and finally, thickness is adjusted by moving the platform or the recoater device [6]. Consolidated parts are then removed from non-bonded particles. Selective cement activation (SCA) is a variation of the binder jetting class of technologies, in which the powder feedstock is composed of a cement mixture activated selectively by the printed liquid [2,10].

Compared to material extrusion, a major advantage of binder jetting is that complex shapes with overhangs can be produced without support structures, due to the fact that the powder bed surrounding the printed part supports it during the layer-by-layer buildup [1,11–13]. For the same reason, there is no need to optimize the complex rheological and setting behavior of the feedstock such as in material extrusion [1,14]. However, a drawback of using a powder feedstock, instead of a paste, is that the reacted material typically shows a large volume of residual porosity [13,15,16]. Furthermore, the particle size distribution and the reactivity of the powder need to be tailored considering also the flow behavior of the mix [2,16].

Setting time is a limitation for the type of cement used by this technique and geopolymer-based and magnesium-based cements are good candidates for the particle bed binding process [7,10,14,17,18].

Magnesium phosphate cement (MPC), the material used in the present study, is a good candidate due to its quick setting time, good mechanical strength and durability. Furthermore, the printed activation liquid is tap water, which simplifies the processing. In comparison, for the magnesium oxychloride cement used in other studies, chlorine is typically added through a solution of magnesium chloride in the jetted water [14,17,19], and the resulting binder is non-hydraulic.

Process manufacturing parameters can be described according to the three printing steps described earlier. A powder bed layer is generated by traversing the recoater at a specified speed [8]. The layer thickness is defined as the height of the generated powder layer in the Z-direction (direction of layer stacking) [8]. The layer thickness is a variable parameter that in principle can be freely set in the process, but in practice is linked to other feedstock and process properties (e.g. the maximum particle size present or the flowability of the mixture). Indeed, several previous works in particular suggested that the minimum layer thickness should be higher than the largest particle size in the powder mixture [20,21]. A smaller thickness provides better resolution and surface quality, but, conversely, it increases processing time [22,23].

In a selective cement activation (SCA) system, the printhead moves over each deposited layer with a given velocity to dispense drops of the liquid activator with a specified flow rate [24]. The total volume of a job box is meshed in a bitwise manner into voxels, which is the three-dimensional equivalent of pixels [17,25].

The amount of water printed in each voxel is optimized based on voxel size, powder bed density and printing speed [17,25] and amount of water required to complete the setting reaction. The fluid flow rate can be controlled by the pressure behind the solenoid valve and/or by the signal frequency [17,25].

The process can be operated with continuous printing, i.e., opening and closing the valves only at the beginning and end of the object's cross-section, or with drop-on-demand printing, i.e., opening and closing the valves at a given frequency to generate single drops.

In the first case, a 3D object is printed initially by coalescence of "single-line primitives" in the path of a single nozzle, followed by inter-line bonds to create single cross-sections, and inter-layer bonds between successive layers [17,24]. In the latter case (drop-on-demand) a single drop is jetted in a voxel and bonds by diffusion to the other drops along the line path of a single nozzle, between nozzles and between successive layers. The drop-on-demand approach was followed in this work since it can lead to a more homogeneous distribution of the printing liquid and a tighter control on the diffusion of the printing liquid within the powder bed.

SCA manufacturing products have potentially anisotropic properties compared to traditional concrete production methods. The particle (binder plus aggregate) distribution in the powder bed due to the layering process during deposition and their shape, and the liquid distribution related to the droplets' migration behavior within the particles and kinetic energy of droplets, which strongly impacts the bed from the top, are possible sources of anisotropic behavior of the printed blocks when subjected to stresses [13]. The part orientation in the powder bed therefore is a primary parameter to assess the anisotropic behavior of cementitious parts [25–27].

1.1. Aim and concept of the investigation

This work aims at identifying the significant printing parameters for SCA using magnesium phosphate cement and silica sand aggregate. A regression model between printing parameters and flexural and compression strength is used to illustrate a systematic relationship between multiple inputs and key outputs. Printing parameters (inputs) that can be controlled at two separate levels are printing speed, layer thickness, raster angle and build orientation. A screening step was designed to understand the effect of the aforementioned factors on flexural and compression strengths (outputs) using analysis of variances (ANOVA).

2. Experimental program, materials and methods

2.1. Material and mixture composition

The powder blend for the SCA process was a mixture of aggregate and binder materials. For this study, the feedstock was commercially provided by Desamanera Srl (Rovigo, Italy) and the composition was a mixture of magnesium oxide (MgO, CCM grade, RHI Magnesita GmbH, Vienna, Austria), potassium phosphate (KH_2PO_4, MKP, agricultural grade, Agri 2000 Italia srl, Ferrara, Italy) and silica sand (Bacchi SpA, Boretto (RE), Italy; particle size distribution between 0 and 2 mm). The ratio binder/aggregate in the powder bed was 50 % by mass. The activator solution to initiate the cement reaction was deionized water at room temperature.

2.2. Manufacturing and test methods

2.2.1. 3D printing process

The test specimens for experimental investigations were printed with a DESA1 printer (Desamanera srl, Rovigo, Italy). The recoater and printer were both mounted on the same gantry; the powder mixture was stored in hoppers, and each layer was deposited in a reciprocal movement.

Each layer was deposited with two passes of the recoater, each depositing half of a layer thickness. Nozzles are installed on a same gantry as the recoater is, therefore in reality the process initiated by spreading powder in a half of a determined layer thickness in X-direction. The water was jetted after the first pass, i.e. in the middle part of each layer, and immediately after water spraying another half of the layer was deposited (in the -X direction). The technique used allows for the immediately arrival of dry powder onto the wetted zone, adding the initially missing direction for water diffusion (upper direction on the Z-axis) and creating a stronger connection between consecutive layers.

Hydrostatic pressure in the reservoir tank supplied water flow to the tubes and valves. Two hundred sixty-four nozzles (internal diameter = 1.1 mm) were installed on the printhead at a distance of 5.7 mm from each other and in a single row, dispensing the required water drop mass. For the utilized machine, the drop mass was a function of the control signal duration, and the opening time was adjusted in the DESA1 slicer software, D-slicing (Desamanera srl, Rovigo, Italy). Printed specimens were kept in the powder bed after printing for one day at room temperature, to ensure a sufficient handling strength. Mechanical tests were carried out on samples six months after printing.

The printing parameters could significantly affect the mechanical

strength of printed specimens. Effects of "printing speed", "layer thickness", "raster angle" and "build direction" on flexural and compression strength were studied in this work. According to EN 196-1 standard [28], prisms with dimensions 40 × 40 × 160 mm^3 (W × H × L) were printed for bending strength determination and compressive strength tests. Cylinders (diameter 60 mm, height 40 mm) were printed to investigate the shape accuracy and determine the printer's resolution. Based on the DOE principles [29], the experimental procedure was designed to point out the effect of the inputs, as summarized in Table 1.

The printing process factors that the operator can control were selected among all variables. CAD files of the specimens were designed by Solid works® and transferred to the proprietary slicer software. "Layer thickness" and "printing speed" were two parameters that could be set in the slicer. The values of level "low" and "high" for the printing speed were chosen based on preliminary tests in a typical range that allows for a visually defect-free deposition. The values of level "low" and "high" for the layer thickness are typical values used from user experience in the process, to achieve either higher printing resolution and cubic voxel (5.7 mm) or higher build rate (8.5 mm). The layout of samples in the powder bed was designed using slicer software. The raster angle was adjusted by arranging the workpiece's X-axis to the machine's X-axis (Fig. 2). Nozzles were designed in moduli with 5.7 mm distance.

2.2.2. Fluid drop mass

A voxel can be defined as the smallest printed unit volume. In this process, this corresponds to the smallest volume into which a single drop of water is jetted. The printed 3D object can be seen as an assembly of single voxels, therefore the properties calculated for a single voxel (e.g. the water/cement ratio) can be extended to the whole part.

Referring to the machine coordinate system (Fig. 1), a voxel was determined by three components: 1) jet-jet distance in Y-direction (equal to 5.7 mm - constant), 2) layer thickness in Z-direction and 3) distance between two consecutive drops along the X-axis (X.dim, kept constant equal to 5.7 mm).

The amount of water jetted in each voxel was calculated as the amount needed for a stoichiometric reaction of the cement.

There are three reactants for the magnesium phosphate cement reaction (equation (1)(1)) [30]:

$$MgO + KH_2PO_4 + 5H_2O \rightarrow MgKPO_4.6H_2O \quad (1)$$

where MgO and KH_2PO_4 were in the powder bed, and the H_2O was sprayed from the printhead.

The mass of water per voxel (β), in the following referred to as "drop mass", can now be calculated from the stoichiometry of water to dry cement "s" (equal to 0.51), the ratio of cement components to powder feedstock- (α, equal to 0.5 in this study), and the density of the powder bed (ρ_{pb}):

$$\beta = \text{Voxel}\ \rho_{pb}\ \alpha\ s \quad (2)$$

where Voxel is the volume of a voxel.

A hydrostatic mechanism in the reservoir tank supplied the pressure at three levels. All samples were printed with a medium pressure level (constant during printing), therefore the mass of water per voxel β was adjusted by modifying the nozzle opening time (OT) in the slicer software. The opening time was adjusted by trial and error until obtaining an average mass equal to β for each valve opening (equivalent to one drop). The used values are shown in Table 3.

It needs to be considered that there is a maximum opening time determined by:

$$OTmax = X.dim / S_{print} \quad (3)$$

Where S_{print} is the velocity of the printhead. This is the time that it takes for the printhead to travel between two voxels, which obviously is an upper limit for the valve opening time.

During a mock printing it was verified that the multiplication of β by the number of solid voxels for each part reflected the mass of water printed in the part, measured directly by a digital balance (accuracy = 0.01 g), within a deviation of 3 %.

Table 1
DOE table of studied printing factors.

Label	Factor	Unit	Level	
			Low (−1)	High (1)
A	Printing speed	mm/s	20	80
B	Layer thickness	mm	5.7	8.5
C	Raster angle	grad	0°	90°
D	Build direction	–	Z	Y

Table 2
Results of powder bed density.

Label	Velocity of powder spread [mm/s]	ρ_{pb} [g/cm^3]	Standard deviation
V1	20	1.52	0.018
V2	50	1.50	0.024
V3	80	1.56	0.019

2.3. Design of experiment (DOE)

A screening DOE with fraction factorial design was applied to evaluate the effect of printing parameters on the flexural and compressive strengths. Using the generator I = ABC ($2_{IV}^{(4-1)}$), a two-level fractional factorial plane (FFP) in three treatments was designed. Each parameter investigated at two levels includes: high (+1) and low (−1) that were reported in Table 1; low and high values of each level were determined based on the feasibility of the machine to print dimensionally acceptable samples. DOE and ANOVA analysis (Analysis of Variances) were performed in the RStudio software [31]. In this study, the crucial P-value was set at 95 percent confidence level or 5 percent significant level.

2.4. Tests

2.4.1. Powder bed characteristics

A preliminary step before the printing process was to measure the powder bed density (ρ_{pb}), which was essential to calculate the fluid drop mass. The powder bed density is governed by the powder blend characteristics and by the layer generation mechanism. Since the characteristics of the materials (type of aggregate and particle size) were constant in this research, the powder spread velocity was the only parameter influencing powder bed density. Hence, ρ_{pb} was measured at three levels, 20, 50 and 80 mm/s.

The measurement of ρ_{pb} was carried out by printing cups with inner size of 50 × 50 × 50 mm^3 and 30 mm wall thickness (Fig. 3). Printed cups were weighed with and without the deposited powder inside, and the inner volume of each printed cup was measured by a caliper. For each "spread velocity" level, three repeats were carried out.

2.4.2. Flexural strength and compression test

Compressive and flexural strengths were determined on 40 × 40 × 160 mm prisms. Referring to Table 4, three specimens for each set of parameters were printed. Tests were conducted on a Toni Technik Model 1544 (Berlin, Germany) mechanical testing machine equipped with three-point bending and compression jigs, according to DIN EN 196-1 standard [28]. The distance between loading points for three-point bending test was 120 mm. The compressive strength was measured on the broken samples from the three-point bending test.

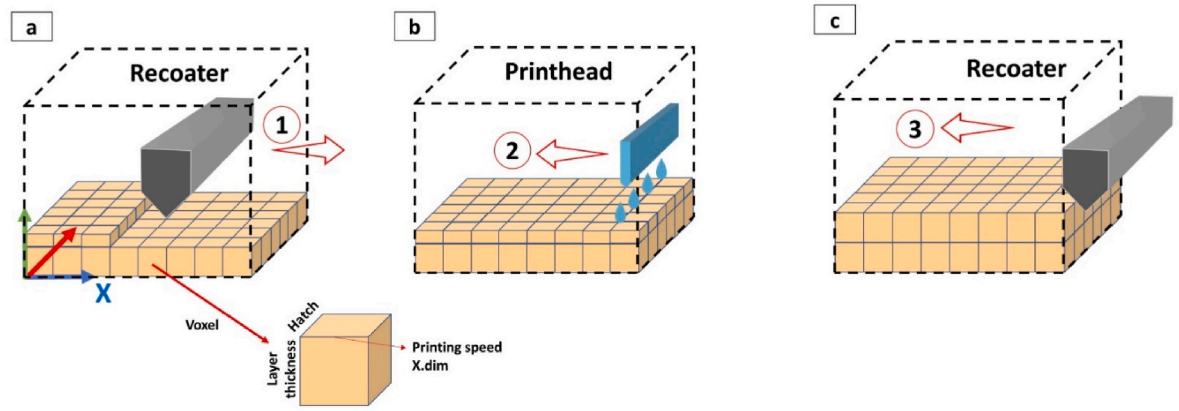

Fig. 1. Schematic of printing process a) powder deposition for half of a layer, b) jetting of activator solution, and deposition of second half a powder layer.

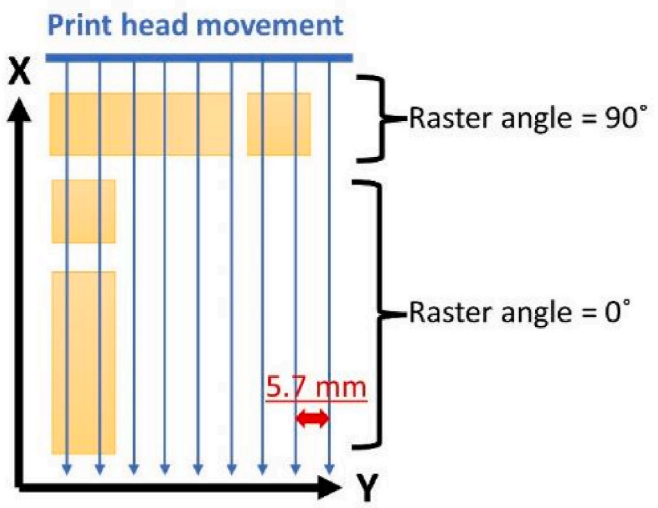

Fig. 2. Samples layout in the powder bed.

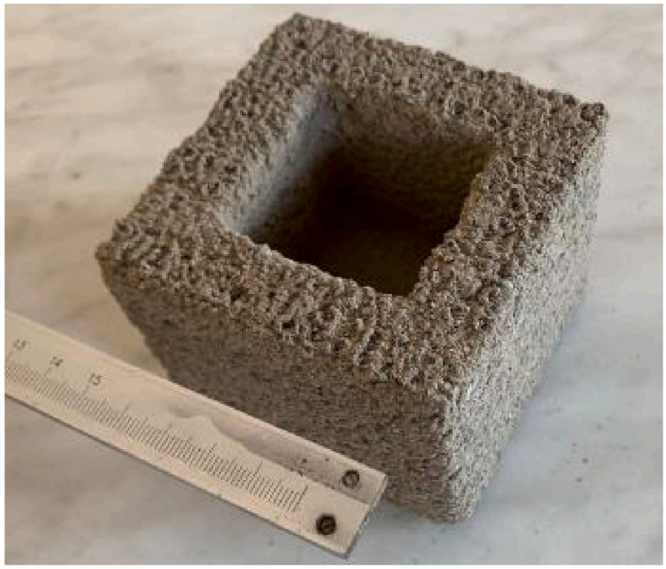

Fig. 3. Powder bed density cup.

Table 3
Binder drop mass and opening time.

No.	Printing Speed [mm/s]	Layer thickness [mm]	Opening time [ms]	drop mass per voxel [g]
1	20	5.7	22	99.3
2	90	5.7	22	99.3
3	20	8.5	30	148.9
4	90	8.5	30	148.9

3. Results and discussion

3.1. Powder bed density and binder drop mass

Table 2 shows the measured values for ρ_{pb} at different spreading speeds. The operated machine has no compaction mechanism (vibration or roller system) and the Tukey test plot (Fig. 4) reveals, with a confidence level of 95 %, that the powder spread velocity is not a significant factor in determining the ρ_{pb} for the interval under study.

The slight increase of the mean value of ρ_{pb} between V = 50 mm/s and V = 80 mm/s can possibly be related to the amplified vibration in the printer. As the spindle and axes motors rotated, the recoater vibrated at frequencies of the motor's rotation. Higher recoater speed increased the shaking of the powder blend, slightly improving the powder discharge from the hopper.

In order to calculate β (mass of water per voxel), it is required to have the powder bed density. The real powder bed density has a value between tap and apparent density of the powder feedstock, and in this research, powder bed density was determined empirically. Powder spreading parameters such as velocity and aggregate particle size affect the final density or target density of products. Powder bed density also shows the effects of these parameters. With the machine in hand the only parameter to change the powder bed density was velocity of powder spread, and statistical analysis revealed that effect of this factor was not significant, therefore a value of ρ_{pb} = 1.50 g/cm^3 was used in the calculation of the drop mass (β) according to Equation (3). The effect of spreading parameters on the properties of final products can be evaluated by the final density of parts instead of powder bed density.

The OT obtained experimentally to achieve the calculated β was then set in the slicer software. The values of the experimentally determined opening times adjusted on the calculated drop mass per voxel are summarized in Table 3.

3.2. Flexural strength and compression test

Table 4 shows the flexural and compression strength results of the tested samples. ANOVA was used to evaluate the obtained data to identify important factors for the 3D printer in use.

Table 4
DOE table for screening and results.

Run.number	Treatment	Factor				Response	
		Printing speed (A)	Layer thickness (B)	Raster angle (C)	Build direction (D)	Flexural strength [MPa]	Compressive strength [MPa]
1	1.1	−1	−1	−1	−1	1.08	1.81
2	1.2	−1	−1	−1	−1	1.30	1.94
3	1.3	−1	−1	−1	−1	0.94	1.75
4	2.1	1	−1	−1	1	1.38	2.38
5	2.2	1	−1	−1	1	1.52	2.44
6	2.3	1	−1	−1	1	1.42	2.94
7	3.1	−1	1	−1	1	1.20	2.25
8	3.2	−1	1	−1	1	1.28	2.81
9	3.3	−1	1	−1	1	1.02	2.25
10	4.1	1	1	−1	−1	1.69	2.25
11	4.2	1	1	−1	−1	1.28	2.31
12	4.3	1	1	−1	−1	1.30	2.31
13	5.1	−1	−1	1	1	0.93	1.75
14	5.2	−1	−1	1	1	0.81	2.38
15	5.3	−1	−1	1	1	0.93	2.25
16	6.1	1	−1	1	−1	0.96	2.00
17	6.2	1	−1	1	−1	0.91	2.63
18	6.3	1	−1	1	−1	0.94	2.13
19	7.1	−1	1	1	−1	1.25	2.00
20	7.2	−1	1	1	−1	1.05	2.13
21	7.3	−1	1	1	−1	1.23	2.13
22	8.1	1	1	1	1	1.18	2.75
23	8.2	1	1	1	1	1.10	3.00
24	8.3	1	1	1	1	1.15	2.94

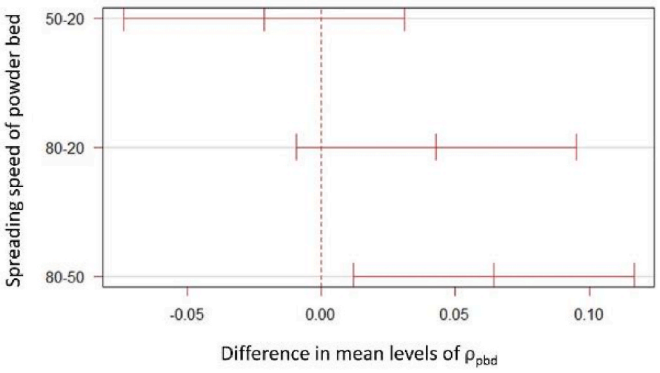

Fig. 4. Tukey's test to compare differences in the measured ρ_{pb}.

3.2.1. Analysis of variances (ANOVA)

Flexural and compressive strengths were the responses to the variables screened as printing parameters, including printing speed (A), layer thickness (B), raster angle(C) and build direction(D). The linear regression models:

$$\frac{1}{Flexural\ strength} = 0.90 - 0.19A + 0.02B + 0.21C + 0.16AC - 0.21BC \quad (4)$$

$$Compressive\ strength = 1.80 + 0.39A + 0.23B + 0.39D \quad (5)$$

were obtained from the ANOVA to determine significant factors and their interactions. Table 5 and Table 6 show the ANOVA results only for the key factors. The full models are reduced to statistically significant factors to prevent the overfitting of data [32]. The predicted strengths (flexural/compressive strength) for a given set of input parameters are found by substituting the coded level of each factor (Factor levels are orthogonally coded, −1 or 1) into the corresponding obtained model (equations (4) and (5)).

As an example, if a designer intends to print a sample with printing speed = 90 mm/s, layer thickness = 8.5 mm, raster angle = 90°, and build direction = Y, all printing parameters are at a high level, then inserting 1 in equation (4) will estimate the flexural strength.

Residual plots and probability plots are used to check the model adequacy. A Quantile-Quantile plot, often known as a Q-Q plot, is a scatter plot that compares two sets of data; Q-Q plots are commonly used to evaluate if a set of data probability came from a particular theoretical distribution. Plotting the sample quantiles against a normally distributed data set can be used to assess the normality assumption. A straight line should be drawn when plotting the second quantiles that have a normal distribution. The quantile-quantile plots (Fig. 5- A and B) reveal that the points for each model can be fitted by the straight line (red line); therefore, both sets of theoretical and sample quantiles come from the same distribution for flexural and compression models [32–34].

Another standard method of evaluating model adequacy is the analysis of model residuals, where a residual is the difference between the measured value and the model predicted value for a particular set of input parameter values. As estimates of the true error, model residuals should have the same qualities as those of the true error, such as being random, independent, and uniformly distributed with a mean of zero and constant variance. The ratio of the model residual to its standard deviation can be used to normalize residuals. The "residuals versus fits plot" was used to evaluate the model's adequacy, and it shows a scatter

Table 5
ANOVA table for flexural test.

Factor	Degree of freedom	Sum of squares	F-value	P-value
A	1	0.065	8.719	0.008
B	1	0.095	12.768	0.002
C	1	0.201	27.179	5.8e-5
A:C	1	0.042	5.682	0.028
B:C	1	0.075	9.352	0.007
Residuals	18	0.266	NA	NA

Table 6
ANOVA table for compression test results.

Factor	Degree of freedom	Sum of squares	F-value	P-value
A	1	0.893	17.577	0.0004
B	1	0.310	6.111	0.0225
D	1	0.940	18.500	0.0003
Residuals	20	1.016	NA	NA

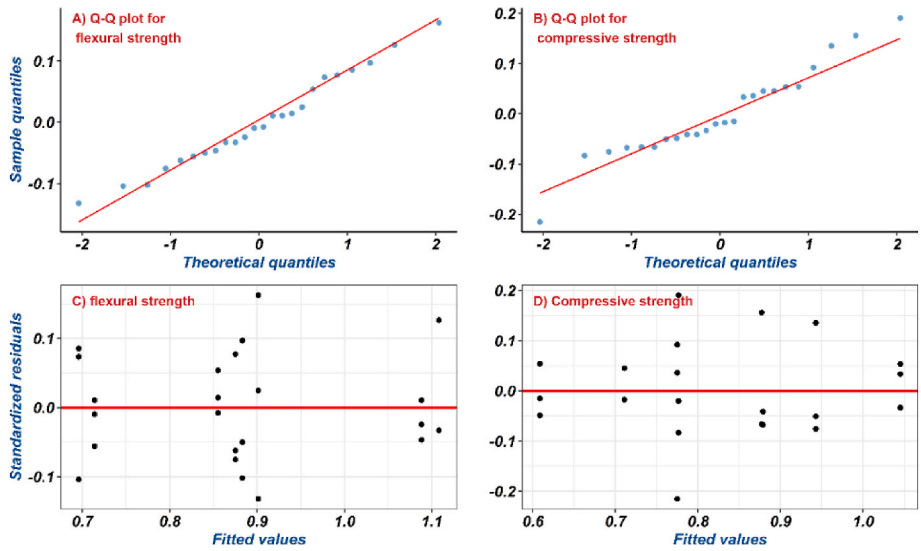

Fig. 5. A and B) QQ-plots for each of the flexural and compressive models (equations (4) and (5)), C and D) Model standardized residuals plotted as a function of linear models.

of residuals about zero with no pattern for both models (Fig. 5C and D) [35]. It is acceptable to draw the conclusion, after evaluating both the residual and the probability plots, that both models are adequate for further investigation [32–34].

3.2.2. *Main effect plots*

Among all input factors for flexural strength, "printing speed" (p-value = 0.007), "layer thickness" (p-value = 0.014) and "raster angle" (p-value = 9.58e-05) were significant. For compressive strength, "printing speed" (p-value = 4.4e-04), "layer thickness" (p-value = 0.022) and "build direction" (p-value = 3.4e-04) revealed significancy.

The main effect plots of designed parameters at each level are shown in Fig. 6. In the following paragraphs, the effect of each factor is discussed in detail.

3.2.2.1. *Printing speed.*

"Printing speed" showed a significant effect on both responses with p-value = 0.010 for flexural strength and p-value = 0.001 for compressive strengths, indicating a larger significance of this factor when considering compressive forces. Setting the printing speed at a high level led to better mechanical strength (Fig. 6). The mechanical strength of printed parts is proportional to the volume of cementitious bonds formed among the aggregates ($\sigma_{max} \sim V_{cementitious\ bond}$) [8,36]; so the physical interpretation of printing speed can be related to the powder binder interactions (PBI), where the droplet jetting path can be altered by changing the droplets velocity.

The total velocity of a droplet is oblique, as schematically illustrated in Fig. 7-A, included "drop release speed" and "printing speed". The same drop mass was obtained for low and high level of printing speed (Table 3), but samples with faster printing speed had larger wetted areas

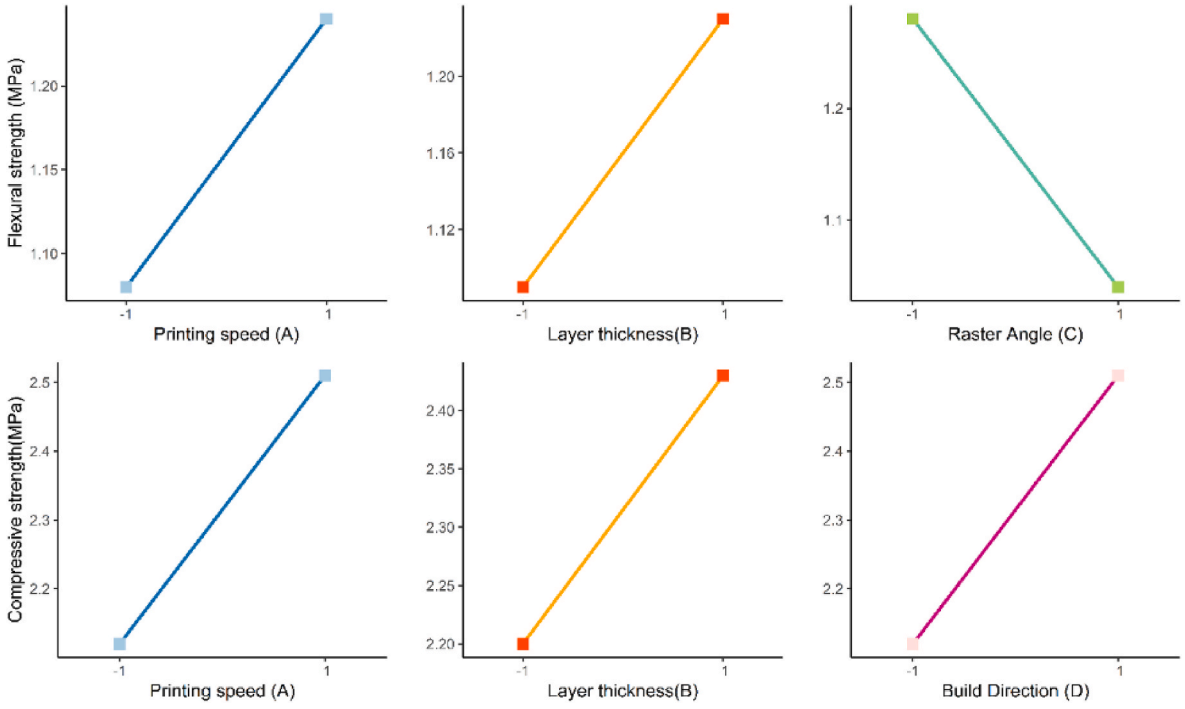

Fig. 6. Main effect plots of significant printing factors on flexural and compressive strengths.

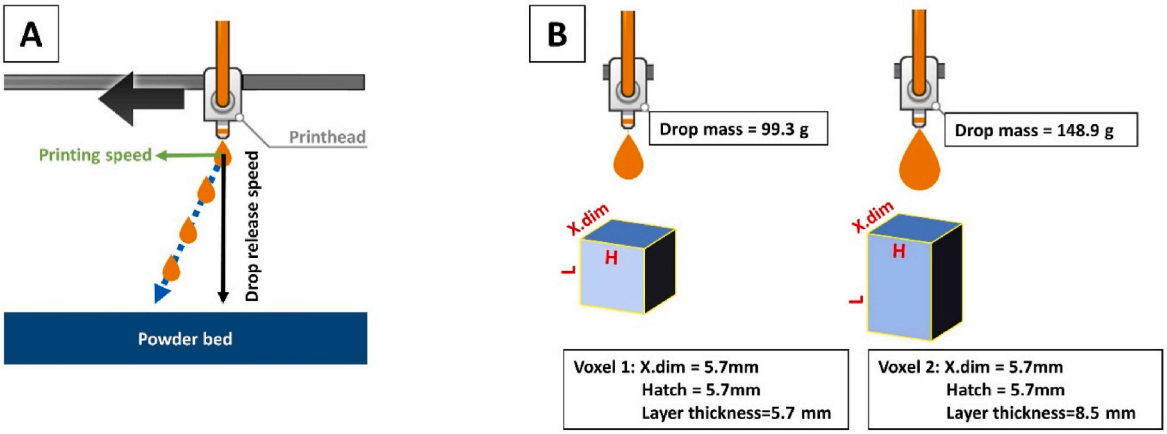

Fig. 7. Schematic graph of the impinged droplets from the print head. (A) Overall velocity of a single droplet and its decomposed orthogonal components. (B) Schematic of dripped droplet on the surface of two voxels with different layer thickness.

and less vertical penetration; thus, the macro defects were limited and the imbibition process (fluid migration through porous media under gravity and capillary forces) was facilitated to form more homogeneous cementitious bonds within the target volume, and thereby better mechanical properties were obtained.

3.2.2.2. Layer thickness. The layer thickness was another significant printing parameter that contributed to higher mechanical strength in both the flexural (p-value = 0.014) and compressive (p-value = 0.022) tests (Fig. 6).

Specimens designed with a high layer thickness (8.5 mm) were characterized by approximately one and half times larger volume (Voxel) with respect to those with a lower thickness (5.7 mm); consequently, the drop mass ($\beta = \text{Voxel} \times \rho_{pb} \times \alpha \times s$) was increased by 50 % as shown schematically in Fig. 7-B.

Water penetrates vertically and spreads horizontally (imbibition process), and despite of the fact that the designed voxels were rectangular prisms, they were formed in semi-spherical primitive units [37]. The primitive unit's formation will stop once an equilibrium state is reached. Powder-binder interaction in SCA is including both binder cement reaction and water diffusion in a porous media [14]. Once water droplets arrives to the powder bed, MgO particles react at their surface, and MKP particles are dissolved by water [14]. The imbibition process of droplets in a porous media was followed by a drainage step, if there was an excess of liquid. In drainage, water migrated from the saturated region (the initial region that water was penetrated) to the surrounding dry aggregates until the driving force of both regions became equal [38].

Delivering 50 % more water on the top surface of voxels indicated more fluid for the water distribution phases (imbibition and drainage), which wetted more aggregates to initiate the hydraulic reaction. Furthermore, a bigger amount of water had greater gravitational forces to penetrate vertically during the imbibition process. On the other hand, the impact of the droplet with greater force generated larger defects onto the powder bed. So, with higher layer thickness, the predominance of the increase in the cementitious bonds volume against the corresponding defect generation, has determined the higher flexural and compression strength of the printed parts.

3.2.2.3. Build direction. "Build direction" was the most significant parameter considering compressive strength (p-value = 3.4e-04). This qualitative factor assessed the anisotropy of the printed materials' mechanical characteristics. The flexural strength was evaluated in two different orientations: one perpendicular to the top surface of the sample (considering the top surface as the X–Y plane and the force direction as -Z), and the other parallel to the top surface (with the force direction as Y). The experiment for the second test involved rotating each sample by 90° along the longitudinal axis prior to its execution. This method involved testing sensitive layers that are aligned with the maximum stress to evaluate how the build direction affects the properties of the final product.

The coded factor levels −1 and 1 were related to test direction normal to X–Y (Fz) and Z-X (Fy) planes, respectively (Fig. 8). ANOVA of the build direction factor effect on the flexural strength gave the p-value = 0.99, which was less than the 5 percent significance level; consequently, this factor was negligible.

Particle size distribution and low powder compaction during the layer generation step, as well as grooves generated by jetted water, dissolution of binder (MKP and MgO) particles and water penetration process during jetting liquid, cause significant residual porosity in the printed blocks [14,39]. The microstructure produced during printing can be identified as a network that is a function of build direction [40].

Compared to the traditional concrete (cast-in-place), a hardened 3D-printed part has been shown to typically possess two distinct types of interfaces [41]. The first type of interface is related to the joint between primitive units or inter-voxel connections (i.e. connections among adjacent voxels within the same layer), and the second type of interface is between successive printed layers (Fig. 8-A). Depending on the printing parameters, different powder binder interactions (PBI) occur, and it could be inferred that the interfacial bond strength was related to local changes in porosity [41].

Fig. 9-A shows visible layering in the Z-axis direction, with distinct bright and dark bands denoting inter-layer connections. A cross mark signifies distinct layers, while a yellow line identifies two different bands for the fifth layer. According to Lowke et al. [2], dark and bright bands indicate dense and loose materials with voids. Therefore, a printed product can be identified as an orthotropic laminar composite with dense (Fig. 9 — dark band) and loose (Fig. 9- bright band) materials. Schematic of laminar composite materials for each single-line primitives is provided in Fig. 8. Impact zones of water droplets in the center of the voxel and the dissolution of binder materials are main source of microporosities depicted as bright band in Fig. 8-A. Gobbin et al. [14] using the same printer and studying the microstructure of materials with similar voxel size, reported that the porosity in the middle of the voxel, where droplets are ejected, forms a network which is compatible with the current survey results.

Specimens subjected to Fz were fragmented because compressive stresses were applied to the loose material, and specimens were fractured at different points. Conversely, forces normal to the Z-X plane (Fy) were applied to the relatively dense layers and delaminated the specimens in inter-layer connections. For instance, delaminated layers under compression were observed for sample 8.1 (Fig. 9-B and Fig. 9-C).

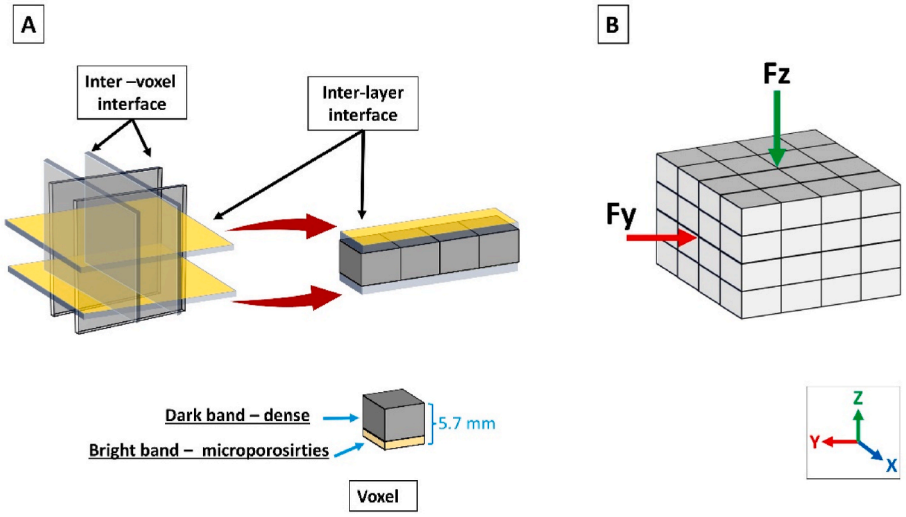

Fig. 8. Schematic diagram of loading directions and interfaces between primitive single-lines and layers.

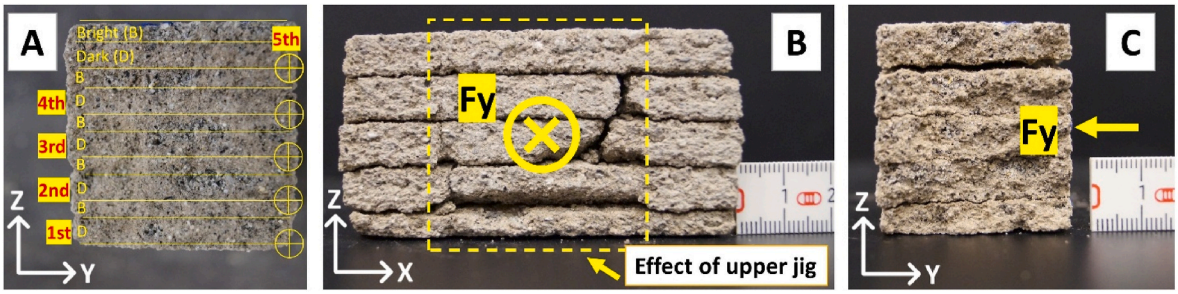

Fig. 9. A) visible layering of printed part, within the Z direction, B) delamination of specimen under compression stresses – top view and the effect of upper jig C) delaminated printed layer under compression stresses – side view.

3.2.2.4. Raster angle. The raster angle was the most significant parameter, while the flexural strength was the considered response (p-value = 9.5e-05). Printed sample with raster angle = 0° showed better flexural strength with respect to those printed with raster angle = 90° (Fig. 6). Once the compression test results for ANOVA were considered, the p-value was 0.58, indicating that the raster angle was not significant.

A "single-line primitive" is formed by the coalescence of single voxels in the path of a nozzle, and adjacent lines merge together to create a cross-section [24]. In other words, the raster angle is the angle between the single-line primitive and the X-direction of the printed sample (workpiece coordinate system); altering raster angle changes the orientation of the "inter-voxel connection" between single-line primitives. Using a printhead with a fixed distance between each of the nozzles, parts may be positioned within the powder bed with respect to the global X-direction (coordinate system of the printer/CNC) to achieve various raster angles.

Observing the test specimens' break pattern is useful in evaluating the effect of the "raster angle" on the flexural strength. The break pattern for samples with 0° raster angle (sample 1.1 in Fig. 10-A) showed pronounced step cracking, indicating the presence of lower strength interfaces where the initiation of the crack was at more than one point followed by crack deflection. Conversely, the sample coded as 5.2 (Fig. 10-B) that was printed with a 90° raster angle showed a vertical crack under bending stresses; the crack initiated from void spaces –porosity– in the middle of the bar and propagated directly to the bottom of the sample. It could be interpreted that the raster strategies affect porosity orientation in a printed block, as it alters the direction of inter-voxel interfaces respect to the applied forces. In particular, the interface between voxels in the printing direction (X) is stronger than the interface

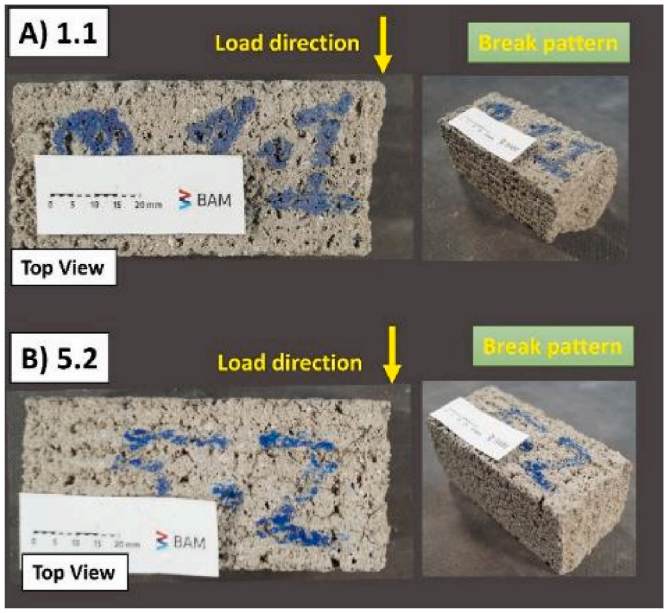

Fig. 10. Test specimens after bending tensile strength testing with noticeable differences in the crack pattern of the prism. A) sample 1.1 - raster angle = 0°, step cracking and B) sample 5.2 - raster angle = 90°, vertical cracks.

formed between nozzles (Y direction).

3.2.3. Interaction plots

ANOVA of flexural strength regression model reveals significance for interactions between factor A-C (p-value = 9.4e-03) and B–C (p-value = 0.036). The interactions between the discussed factors are plotted in Fig. 11. High levels of "printing speed" and "layer thickness" with "raster angle" parallel to the powder bed are recommended to achieve optimum flexural strength. When designers consider the flexural strength criterion, the orientation of components in the powder bed (build direction factor) is negligible. The latter conclusion is key when it comes to arranging parts in the build box.

3.3. Shape accuracy

In Fig. 12 target shape (CAD file) and the actual shape (printed part) of a disc with diameter of 60 mm and thickness of 40 mm are compared to identify the resolution of the printer. Captured images were converted to bitwise binary with ImageJ [42] software for image analysis.

Fig. 12-A shows the top view of the printed disc. The cross marks represent the corners of the designed voxels, and the red circle indicates the CAD target geometry. The top view of the printed geometry can be approximated with a regular hexagon (green dash lines) The circumscribed circle (about 35.3 mm diameter) around the semi-polygon geometry is plotted with blue color. Fig. 12-B shows a half-section of the side view of the same sample. The target geometry in this section is depicted with a red box.

Fig. 12-A indicated that the machine's resolution in X and Y directions was limited by the Voxel sizes. Hatch distance was limited by the nozzle arrangement on the printhead, which was a constant value equal to 5.7 mm. The excessive height of the sample might be partially explained by the fact that an extra layer of powder was deposited at the end of the printing process to prevent water evaporation, leading to oversize the shape in the Z direction due to water diffusion in the layer.

Fig. 12-B shows extra material outside of the target geometry. Binder bleeding causes the printed component to enlarge on the bottom and sides. Depending on the final application, post-processing of the structures may be necessary to achieve the desired tolerances and surface finish. It should be noted, in any case, that the resolution of a printed part depends on several factors, including: powder size distribution, binder reaction rate, evaporation rate, wettability of the particles by the liquid, or liquid diffusion rate. Therefore, different feedstocks and binder systems will give different results in terms of printing accuracy, independently of the specific nozzle dimension and of the fixed distance between the nozzles in the printing head.

4. Conclusions

This paper addressed binder jetting technology with a large-scale powder bed system to produce cement-based materials. A 2^3 fraction factorial experimental design was used to study the effect of process parameters on flexural and compressive strength and statistical analysis (ANOVA) was used to analyze the data. The following conclusions can be drawn.

- The drop mass for the selective cement activation (SCA) process was formulated as "$\beta = Voxel\,\rho_{pb}\,\alpha\,s$" (see eq. (2)). A pre-processing step (in order to determine ρ_{pb}) was to identify the powder bed density that can be determined experimentally by printing a cup and subtracting the weight of the unbonded powder blend inside it from its volume.
- Printing speed and layer thickness were significant factors for the flexural and compressive strengths. A higher printing speed altered the droplet jetting path that can wet more powder feedstock reducing the droplet vertical penetration bringing about stronger samples due to the more homogeneous cementitious matrix and the fewer macro defects induced by water droplet/powder interaction. For a larger layer thickness (or in other words, a larger volume of a voxel), the volume of dispensed water was increased, which facilitates cement reaction and migration of fluid into the porous media leading to higher macroscopic strengths This effect is predominant compared to the generation of larger defects in layers due to application of bigger droplets.
- Raster angle is the most significant factor for the flexural strength, but it did not show significance under compressive forces. Residual porosities in a printed block form a network in specific locations defines as inter-layer and inter voxel interfaces. Under flexural stresses, the interfaces between single-line primitives are sites with lower strength where fracture initiation occurs. This is not observed in the compressive strength determination as the specimen is loaded symmetrically.
- Build direction was the most significant factor for compressive forces, even though it was not a significant factor when flexural strength was the criterion. The build direction was an indicator of the materials' anisotropic behavior. SCA parts were hardened by merging voxels and connecting successive layers, where inter-voxel and inter-layer interactions were identified. As the binder migrated to the bottom, each layer, including loose and dense components, became a laminar composite. Inter-layer interfaces predominantly caused anisotropy; samples subjected to loads parallel to the build direction were more resistant to compressive tensions.

CRediT authorship contribution statement

Farid Salari: Writing – review & editing, Writing – original draft, Validation, Software, Resources, Project administration, Methodology, Investigation, Funding acquisition, Formal analysis, Data curation, Conceptualization. **Andrea Zocca:** Writing – review & editing, Supervision, Project administration, Funding acquisition. **Paolo Bosetti:** Supervision, Methodology. **Petr Hlaváček:** Writing – review & editing, Supervision. **Antonino Italiano:** Resources. **Filippo Gobbin:** Writing – review & editing, Resources. **Paolo Colombo:** Writing – review & editing, Supervision. **Hans-Carsten Kühne:** Supervision, Resources. **Vincenzo M. Sglavo:** Writing – review & editing, Supervision, Resources, Project administration, Funding acquisition, Conceptualization.

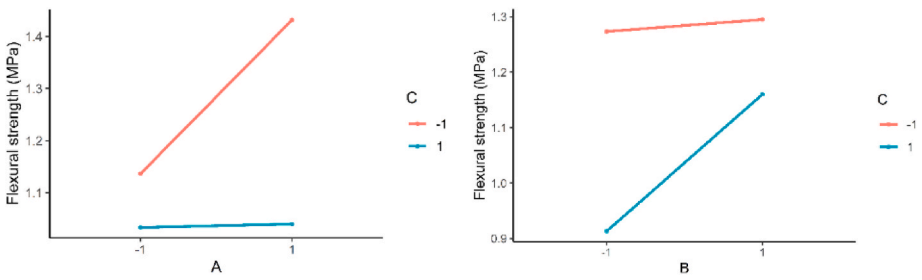

Fig. 11. Interaction plots according to ANOVA for flexural test.

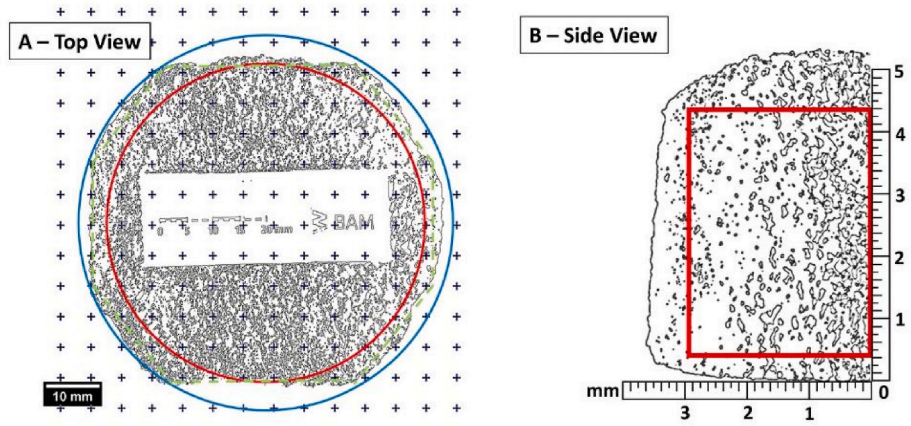

Fig. 12. A) top view of printed disc B) half of side view with camping designed and actual shapes.

Declaration of competing interest

The authors declare that they have no known competing financial interests or personal relationships that could have appeared to influence the work reported in this paper.

Acknowledgment

The authors would like to thank the Desamanera Srl. for their help and kind support in early stages of the project. The authors would also like to express their appreciation to Mr. Andrea Beretta and Ms. Giulia Paciotti for their valuable and constructive help during the printing process of this research work.

The authors received financial support from the Italian Ministry of University and Research (MIUR) within the project Dipartimenti di eccellenza 2018–2022 (Department of Industrial Engineering, University of Trento; project "3D PRINTING") and the JECS Trust grant (Contract no. 2021264).

This study was carried out within the MICS (Made in Italy – Circular and Sustainable) Extended Partnership and received funding from the NextGenerationEU, European Union (PIANO NAZIONALE DI RIPRESA E RESILIENZA (PNRR) – MISSIONE 4 COMPONENTE 2, INVESTIMENTO 1.3 – D.D. 1551.11-10-2022, PE00000004). This manuscript reflects only the authors' views and opinions, neither the European Union nor the European Commission can be considered responsible for them.

References

[1] I. Gibson, D. Rosen, B. Stucker, M. Khorasani, Additive Manufacturing Technologies, Springer International Publishing, Cham, 2021, https://doi.org/10.1007/978-3-030-56127-7.
[2] D. Lowke, D. Talke, I. Dressler, D. Weger, C. Gehlen, C. Ostertag, R. Rael, Particle bed 3D printing by selective cement activation–Applications, material and process technology, Cement Concr. Res. 134 (2020) 106077.
[3] International Organization for Standardization, Additive Manufacturing: General Principles. Part. 2: Overview of Process Categories and Feedstock, ISO, 2015.
[4] R.A. Buswell, W.L. da Silva, F.P. Bos, H. Schipper, D. Lowke, N. Hack, H. Kloft, V. Mechtcherine, T. Wangler, N. Roussel, A process classification framework for defining and describing Digital Fabrication with Concrete, Cement Concr. Res. 134 (2020) 106068.
[5] M. Xia, B. Nematollahi, J. Sanjayan, Influence of binder saturation level on compressive strength and dimensional accuracy of powder-based 3D printed geopolymer, in: Materials Science Forum, Trans Tech Publ, 2018, pp. 177–183.
[6] S. Jones, Additive Manufacturing with Cement-based Materials, (n.d.). https://www.nist.gov/programs-projects/additive-manufacturing-cement-based-materials (accessed January 15, 2022).
[7] M. Xia, J. Sanjayan, Method of formulating geopolymer for 3D printing for construction applications, Mater. Des. 110 (2016) 382–390.
[8] A. Mostafaei, A.M. Elliott, J.E. Barnes, F. Li, W. Tan, C.L. Cramer, P. Nandwana, M. Chmielus, Binder jet 3D printing—process parameters, materials, properties, modeling, and challenges, Prog. Mater. Sci. 119 (2021) 100707.
[9] P. Shakor, S. Chu, A. Puzatova, E. Dini, Review of binder jetting 3D printing in the construction industry, Prog. Addit. Manuf. (2022) 1–27.
[10] P. Shakor, J. Sanjayan, A. Nazari, S. Nejadi, Modified 3D printed powder to cement-based material and mechanical properties of cement scaffold used in 3D printing, Construct. Build. Mater. 138 (2017) 398–409.
[11] M. Casini, Chapter 8 - advanced building construction methods, in: M. Casini (Ed.), Construction 4.0, Woodhead Publishing, 2022, pp. 405–470, https://doi.org/10.1016/B978-0-12-821797-9.00006-4.
[12] S. Shrestha, G. Manogharan, Optimization of binder jetting using Taguchi method, JOM 69 (2017) 491–497.
[13] A. Zocca, P. Colombo, C.M. Gomes, J. Günster, Additive manufacturing of ceramics: issues, potentialities, and opportunities, J. Am. Ceram. Soc. 98 (2015) 1983–2001.
[14] F. Gobbin, H. Elsayed, A. Italiano, J. Adrien, P. Colombo, E. Maire, Large scale additive manufacturing of artificial stone components using binder jetting and their X-ray microtomography investigations, Open Ceram. 7 (2021) 100162.
[15] S. Diener, A. Zocca, J. Günster, Literature review: methods for achieving high powder bed densities in ceramic powder bed based additive manufacturing, Open Ceram. 8 (2021) 100191, https://doi.org/10.1016/j.oceram.2021.100191.
[16] I. Mai, D. Lowke, A. Perrot, Fluid intrusion in powder beds for selective cement activation–An experimental and analytical study, Cement Concr. Res. 156 (2022) 106771.
[17] F. Salari, Binder jet 3D printing of magnesium oxychloride cement-based concrete: a framework to design the rate of voxel, in: Key Engineering Materials, Trans Tech Publ, 2022, pp. 3–12.
[18] H. Elsayed, F. Gobbin, M. Picicco, A. Italiano, P. Colombo, Additive manufacturing of inorganic components using a geopolymer and binder jetting, Addit. Manuf. 56 (2022) 102909, https://doi.org/10.1016/j.addma.2022.102909.
[19] G. Cesaretti, E. Dini, X. De Kestelier, V. Colla, L. Pambaguian, Building components for an outpost on the Lunar soil by means of a novel 3D printing technology, Acta Astronaut. 93 (2014) 430–450.
[20] Z. Zhou, C.A. Mitchell, F.J. Buchanan, N.J. Dunne, Effects of heat treatment on the mechanical and degradation properties of 3D-printed calcium-sulphate-based scaffolds, Int. Sch. Res. Notices 2013 (2013).
[21] K. Lu, W.T. Reynolds, 3DP process for fine mesh structure printing, Powder Technol. 187 (2008) 11–18.
[22] F. Dini, S.A. Ghaffari, J. Jafar, R. Hamidreza, S. Marjan, A review of binder jet process parameters; powder, binder, printing and sintering condition, Met. Powder Rep. 75 (2020) 95–100.
[23] J. Gonzalez, J. Mireles, Y. Lin, R.B. Wicker, Characterization of ceramic components fabricated using binder jetting additive manufacturing technology, Ceram. Int. 42 (2016) 10559–10564.
[24] J.J. Wagner, H. Shu, R. Kilambi, Experimental Investigation of Fluid-Particle Interaction in Binder Jet 3D Printing, 2021.
[25] P.K. Tan, Three Dimensional Printing: Solenoid Value-Jet for Continuous High-Speed Application, Massachusetts Institute of Technology, 2000. PhD Thesis.
[26] P. Shakor, S. Nejadi, G. Paul, N. Gowripalan, Effects of different orientation angle, size, surface roughness, and heat curing on mechanical behavior of 3D printed cement mortar with/without glass fiber in powder-based 3DP, 3D Print. Addit. Manuf. 10 (2) (2021) 330–355.
[27] L. Galantucci, F. Lavecchia, G. Percoco, Quantitative analysis of a chemical treatment to reduce roughness of parts fabricated using fused deposition modeling, CIRP Ann. 59 (2010) 247–250.
[28] E.C. for Standardization, Methods of Testing Cement - Part 1, Determination of strength, 2016.
[29] D.C. Montgomery, Design and Analysis of Experiments, John wiley & sons, 2017.
[30] S.A. Walling, J.L. Provis, Magnesia-based cements: a journey of 150 years, and cements for the future? Chem. Rev. 116 (2016) 4170–4204.
[31] RStudio Team, RStudio: Integrated Development Environment for R, RStudio, PBC, Boston, MA, 2020. http://www.rstudio.com/.
[32] R.R. Chandrasekaran, M.J. Benoit, J.M. Barrett, A.P. Gerlich, Multi-variable statistical models for predicting bead geometry in gas metal arc welding, Int. J. Adv. Des. Manuf. Technol. 105 (2019) 1573–1584.

[33] GR's Website, (n.d.). https://data.princeton.edu/wws509/notes/c2s9 (accessed July 31, 2022).
[34] Understanding Q-Q Plots | University of Virginia Library Research Data Services + Sciences, (n.d.). https://data.library.virginia.edu/understanding-q-q-plots/(accessed July 31, 2022).
[35] 4.2 - Residuals vs. Fits Plot | STAT vol. 462, (n.d.). https://online.stat.psu.edu/stat462/node/117/(accessed July 31, 2022).
[36] R. Ramakrishnan, B. Griebel, W. Volk, D. Günther, J. Günther, 3D printing of inorganic sand moulds for casting applications, in: Advanced Materials Research, Trans Tech Publ, 2014, pp. 441–449.
[37] Y. Bai, C. Wall, H. Pham, A. Esker, C.B. Williams, Characterizing binder–powder interaction in binder jetting additive manufacturing via sessile drop goniometry, J. Manuf. Sci. Eng. 141 (2019).
[38] H. Miyanaji, N. Momenzadeh, L. Yang, Effect of printing speed on quality of printed parts in Binder Jetting Process, Addit. Manuf. 20 (2018) 1–10.
[39] A. Perrot, 3D Printing of Concrete: State of the Art and Challenges of the Digital Construction Revolution, John Wiley & Sons, 2019.
[40] F. Gobbin, H. Elsayed, A. Italiano, J. Adrien, P. Colombo, E. Maire, Large scale additive manufacturing of artificial stone components using binder jetting and their X-ray microtomography investigations, Open Ceram. 7 (2021) 100162, https://doi.org/10.1016/j.oceram.2021.100162.
[41] J. Xiao, H. Liu, T. Ding, Finite element analysis on the anisotropic behavior of 3D printed concrete under compression and flexure, Addit. Manuf. 39 (2021) 101712.
[42] W.S. Rasband, Imagej, Us National Institutes of Health, Bethesda, maryland, usa, 2011. Imagej. Nih. Gov/Ij/.